# Enhanced Human Epidermal Growth Factor Receptor 2 Degradation in Breast Cancer Cells by Lysosome-Targeting Gold Nanoconstructs

**Hyojin Lee,[†,⊥] Duncan Hieu M. Dam,[†,‡] Ji Won Ha,[†,∥] Jun Yue,[†] and Teri W. Odom[*,†,§]**

[†]Department of Chemistry and [§]Department of Materials Science and Engineering, Northwestern University, 2145 Sheridan Road, Evanston, Illinois 60208, United States and [‡]Department of Dermatology, Northwestern University, 676 N. St. Clair Street, Chicago, Illinois 60611, United States. [⊥]Present address (H.L.): Center for Biomaterials, Biomedical Research Institute, Korea Institute of Science and Technology (KIST), 5 Hwarangno 14-gil, Seongbuk-gu, Seoul 136-791, Republic of Korea. [∥]Present address (J.W.H.): Department of Chemistry, University of Ulsan, 93 Daehak-Ro, Nam-Gu, Ulsan 680-749, Republic of Korea.

**ABSTRACT** This paper describes how gold nanoparticle nanoconstructs can enhance anticancer effects of lysosomal targeting aptamers in breast cancer cells. Nanoconstructs consisting of anti-HER2 aptamer (human epidermal growth factor receptor 2, HApt) densely grafted on gold nanostars (AuNS) first targeted HER2 and then were internalized *via* HER2-mediated endocytosis. As incubation time increased, the nanoconstruct complexes were found in vesicular structures, starting from early endosomes to lysosomes as visualized by confocal fluorescence and differential interference contrast microscopy. Within the target organelle, lysosomes, HER2 was degraded by enzymes at low pH, which resulted in apoptosis. At specific time points related to the doubling time of the cancer cells, we found that accumulation of HER2-HApt-AuNS complexes in lysosomes, lysosomal activity, and lysosomal degradation of HER2 were positively correlated. Increased HER2 degradation by HApt-AuNS triggered cell death and cell cycle arrest in the G0/G1 phase inhibition of cell proliferation. This work shows how a perceived disadvantage of nanoparticle-based therapeutics—the inability of nanoconstructs to escape from vesicles and thus induce a biological response—can be overcome by both targeting lysosomes and exploiting lysosomal degradation of the biomarkers.

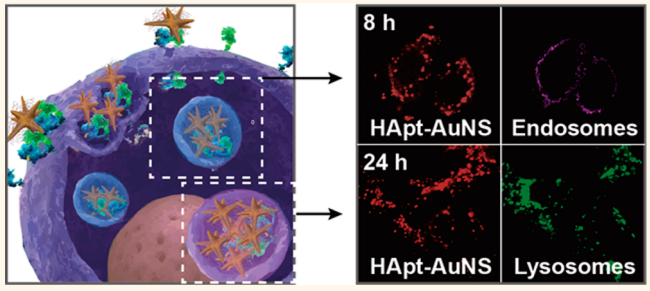


**KEYWORDS:** nanoparticles · targeted drug delivery · gold nanostars · DNA aptamers · lysosomes

Nanoparticle-based delivery systems can improve *in vitro* and *in vivo* efficacies of drugs by enhancing agent stability, internalization in cells, and circulation times.[1,2] In particular, gold nanoparticles (AuNPs) are advantageous in biomedical applications because the surfaces can be readily functionalized *via* gold−thiol chemistry, the core material is biocompatible, and the optical properties can be used to augment diagnostic and therapeutic applications.[3−6] Moreover, anisotropic NPs such as gold nanostars (AuNS) offer benefits over spherical Au colloids in the design of magnetic resonance imaging contrast agents and aptamer drug delivery systems.[7−11] In particular, AuNS synthesized by reducing gold salt with Good's buffer molecules (HEPES) are biocompatible, and thiolated ligands can be released from the tips using ultrafast (fs) light pulses at near-infrared wavelengths.[8,9,12,13] The branched shape of AuNS also results in unique optical properties that enable prospects for imaging in biological conditions[14] and high surface-to-volume ratios compared to spherical AuNPs, which can increase the loading capacity of drugs grafted to nanocarriers.[15,16]

One major challenge in using AuNPs for intracellular diagnostics and therapeutics is the need to escape from vesicular compartments after cellular uptake.[17−19] Typically, ligands that target cell-surface antigens and/or receptors are functionalized on the NP surface to deliver drugs into cancer cells.[1,20,21] As a result, NPs internalized *via* receptor-mediated endocytosis (RME) accumulate in late endosomes and lysosomes,[1,22]

* Address correspondence to todom@northwestern.edu.

Received for review May 22, 2015 and accepted September 1, 2015.

**Published online September 03, 2015**
**10.1021/acsnano.5b05138**

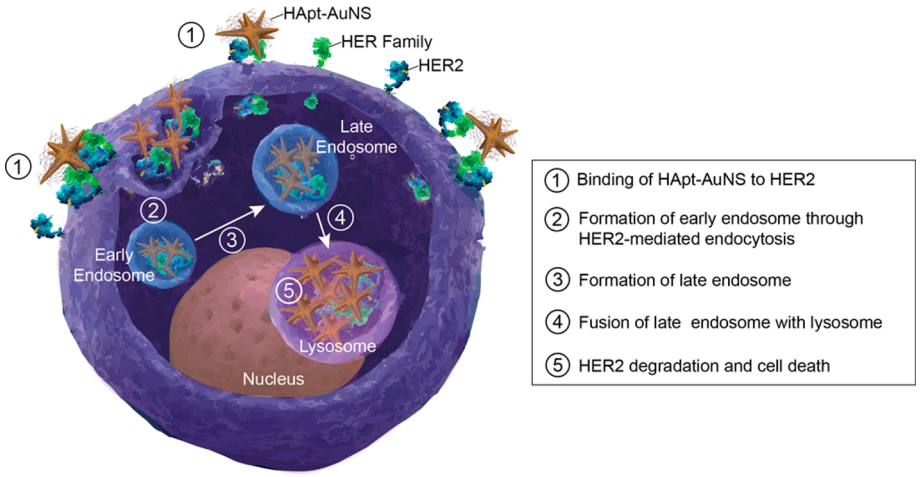


**Scheme 1. Internalization process of HApt-AuNS in HER2-overexpressed cancer cells. HApt-AuNS binds to HER2 on the plasma membrane, and then the HER2-nanoconstruct complex internalizes in the cell by endocytosis. HER2-HApt-AuNS is transported from endosomes to lysosomes, where HER2 is degraded and which induces cell death. Adapted from ref 51.**

which may render drug molecules ineffective from degradation at low pH conditions and enzymes.[17] In contrast, intracellular trafficking of nanoconstructs to targeted endosomes[23] or lysosomes[1,24] can show enhancement of drug bioactivity. Recently, a DNA aptamer with anticancer effects derived from the degradation of human epidermal growth factor receptor 2 (HER2) in lysosomes was reported for gastric cancer cells (N87) and tumors.[25] Since HER2 is expressed 100-fold more on plasma membranes of cancer cells compared to normal cells, this transmembrane protein receptor has been pursued as a target.[26−29] Anti-HER2 aptamer (HApt) is the trimeric version (42 base pairs (bp)) of HER2-specific aptamer, 5′-GCAGCGGTGTG GGG-3′ (14 bp), that was identified by SELEX.[25] HApt has both targeting and therapeutic capabilities, can induce cross-linking of HER2 on cell surfaces, and can result in translocation of HER2 from the plasma membrane to cytoplasmic vesicles with proteases to digest HER2.[25] Downregulation of HER2 can induce apoptosis by altering cell proliferation and downstream signaling pathways.[30,31]

Our hypothesis is that AuNS nanocarriers can increase delivery efficacy of HApt as well as result in increased transport to and degradation of HER2 in lysosomes. We aim to exploit a perceived disadvantage of inorganic nanocarriers—accumulation in vesicular compartments—and use the endocytotic pathway as a means to enhance the response of the targeting drug molecule. Here we show that AuNS nanoconstructs can function as a model system to assess how targeted accumulation and target protein degradation in lysosomes can affect *in vitro* efficacy. We tested HER2 as the well-known biomarker and transmembrane protein in breast cancer cells as well as nanoconstructs of HApt grafted to AuNS (HApt-AuNS). We found that HApt-AuNS showed improved delivery and anticancer effects in targeted cancer cells over free HApt. In order to correlate progression in the endocytosis process with cellular response, we monitored the subcellular localization of HER2-HApt-AuNS complexes using confocal fluorescence microscopy and differential interference contrast microscopy. At the same time points, we measured accumulation of HER2-HApt-AuNS complexes in lysosomes, lysosomal activity, and lysosomal degradation of HER2 and discovered that all were positively correlated. Increased HER2 degradation by HApt-AuNS also triggered cancer cell death and cell cycle arrest in the G0/G1 phase inhibition of cell proliferation.

## RESULTS AND DISCUSSION

Surface-receptor-targeting NPs are usually internalized in cancer cells by receptor-mediated endocytosis,[32] a process involving clathrin-mediated internalization of cargo destined for lysosomal compartments.[1] Scheme 1 illustrates the proposed key binding and trafficking steps for HApt-AuNS in a HER2-expressing cancer cell. The polyvalent nature of HApt in the form of HApt-AuNS can induce cross-linking of HER2 on the cell surface. After binding to HER2, the nanoconstruct can sort HER2 to lysosomes, where HER2 is degraded. The process is initiated when (1) HER2 receptors on the plasma membrane bind to HApt-AuNS nanoconstructs and then (2) HER2-HApt-AuNS complexes are encased by folding of the membrane into a vesicle and then enclosed within early endosomes. As they mature, (3) early endosomes become late endosomes that then (4) fuse with lysosomes. Within lysosomes, (5) HER2 bound to HApt-AuNS is degraded by proteases and acidic conditions, which results in the suppression of cancer cell growth as well as cell death.

**Physical, Chemical, Optical, and *in Vitro* Characterization of Nanoconstructs.** Figure 1a depicts a transmission electron microscopy (TEM) image of anisotropic AuNS, where the average size (tip-to-tip) was 40 nm. This NP size has been

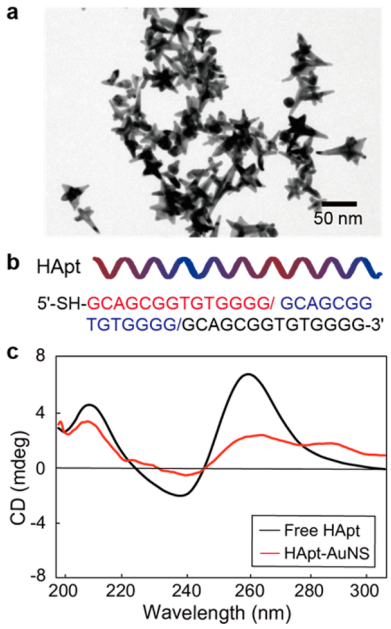


**Figure 1. HApt-AuNS nanoconstruct characterization. (a) TEM image of as-synthesized AuNS. (b) Sequence information on HApt. The color-coding means one unit (14 bp) of trimeric version of HApt (42 bp). (c) CD spectra of free HApt and HApt grafted on AuNS.**

shown to be advantageous for receptor-mediated endocytosis, where 40 nm AuNPs showed higher cellular uptake *via* HER2 receptors compared to 2-, 10-, and 70 nm AuNPs.[33] Using our procedures for attaching other thiolated oligonucleoties,[7,16] we designed HApt-AuNS nanoconstructs by grafting 5′-thiolated HApt (Figure 1b) on AuNS in citrate buffer at pH 3 and characterized their physical and surface properties. As one measure of dense ligand loading on AuNS, we found that the localized surface plasmon (LSP) resonance of HApt-AuNS shifted to longer wavelengths (~820 nm) compared to as-synthesized AuNS (~791 nm) (Supporting Information Figure S1a). Using dynamic light scattering (DLS), we determined that the hydrodynamic size and charge of HApt-AuNS was 90 nm (compared to 40 nm for bare AuNS) and that the surface charge was reduced to −8.05 mV in PBS solution compared to −30 mV of as-synthesized AuNS (Supporting Information Table S1). This less negative value of surface charge can enhance the interaction of nanoconstructs with cells because of the reduced repulsive forces between the negatively charged plasma membrane and AuNS.[34]

Because anticancer effects depend on the quantity of drugs loaded on NPs,[35] we determined the number of HApt on AuNS using a fluorescence assay with Cy3-labeled HApt and examined the structural integrity of HApt using circular dichroism (CD) spectroscopy (Methods). We estimated that the average number of HApt strands on each AuNS was 410 ± 10 (Supporting Information Table S1 and Figure S1b). Figure 1c indicates that free HApt had a linear structure with a strong positive band at 262 nm and weaker negative bands at 240 and 210 nm. The linear structure of HApt (42 bp) is important for polyvalent binding with multiple HER2 since each 14 bp unit has some affinity to HER2.[25] The CD spectrum of HApt-AuNS was similar to that of the free HApt molecule, which indicates that the HApt conformation was preserved on AuNS. In addition, we evaluated the stability of HApt-AuNS nanoconstructs under *in vitro* culture conditions since various serum proteins in fetal bovine serum (FBS)-containing media can destabilize targeting nanoconstructs by nonspecific protein absorption.[36] We tested HApt-AuNS with different concentrations of FBS media (10%, 50%, and 100%) and did not observe significant aggregation (Supporting Information Figure S2).

We used SK-BR-3 (breast cancer cells) as an *in vitro* model system, although previous work on HApt focused on gastric cancer cells[25] because the occurrence of HER2 overexpression in breast cancers is 4 times higher than that in gastric cancers in patients.[37] SK-BR-3 cells also show nearly the same expression levels of HER2 as N87.[38] First, we investigated whether cellular uptake of HApt-AuNS depended on HER2 expression levels by comparing SK-BR-3 (HER2 positive) and normal breast cell lines (MCF-10A, HER2 negative) because HER2 levels in SK-BR-3 are 100 times higher than that in the normal cell line[37] (Supporting Information Figure S3). We found that there was a 2.2 times higher amount of AuNS in SK-BR-3 ($6 \times 10^6$ AuNS/cell) compared to MCF-10A cells ($2.7 \times 10^6$ AuNS/cell), which suggests that internalization of the nanoconstructs depended on the expression level of HER2. To check cytotoxicity of HApt-AuNS on normal cells, we identified the HApt-AuNS concentration for a lethal dose 50 ($LD_{50}$) in cancer cells; 50% cell death was found for 2.5 nM HApt-AuNS (HApt concentration: 1 $\mu$M) in SK-BR-3 cells (Supporting Information Figure S4). To determine whether the nanoconstruct concentration and treatment time were harmful to normal cells, we treated MCF-10A cells with HApt-AuNS for 24 h; however, no cell death was observed (Supporting Information Figures S3b and S5). Cell viability of MCF-10A was maintained at greater than 90% even after 72 h treatment with HApt-AuNS (Supporting Information Figure S5), which suggests that there are minimal adverse effects of the nanoconstructs even after multiple cell-division cycles.[39] We also carried out a competition experiment by blocking HER2 with free HApt (1 $\mu$M) to confirm that HApt-AuNS-induced cancer death was mediated by HER2. After 24 h incubation of cells with free HApt, cancer cell death after HApt-AuNS incubation for 24 h (2.5 nM) decreased *ca.* 20% (Supporting Information Figure S6). This result supported that HApt-AuNS produced anticancer effects in targeted cancer cells since binding to HER2 receptors led to HER2-mediated endocytosis, which ultimately resulted in lysosomal degradation of HER2.[25]

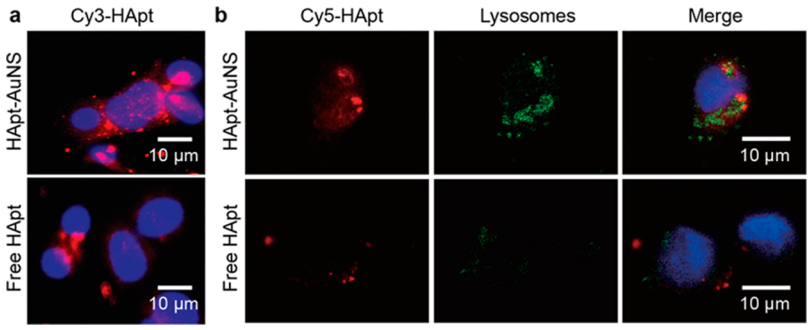


**Figure 2. *In vitro* distribution of fluorophore-labeled HApt-AuNS showed clustering. (a) Cy3-HApt showed higher uptake and clustering when grafted to AuNS in SK-BR-3. (b) Confocal fluorescence images of Cy5-HApt-AuNS, free Cy5-HApt, and lysosomes in SK-BR-3 after 24 h treatment times. The locations of the nanoconstructs overlapped with those of the lysosomes. In all images, the blue color corresponds to DAPI-stained nuclei. The representative images were collected from fluorescence images of three independent experiments ($n$ = 3).**

**Comparison of Uptake for HApt-AuNS *vs* Free HApt.** After confirming specificity of HApt-AuNS to HER2 breast cancer cells, we tested whether nanoconstructs showed increased HApt delivery efficiency. Confocal fluorescence microscopy images show that Cy3 signals from Cy3-HApt-AuNS in SK-BR-3 cells were much higher than those of free Cy3-HApt at the same Cy3-HApt concentration and integration time (Figure 2a). Moreover, the distribution of Cy3-HApt signals was distinct after 24 h, where the Cy3-HApt-AuNS appeared in clusters compared to the lower, diffuse signals of free Cy3-HApt. On the basis of clustering pattern, we hypothesized that nanoconstructs were in vesicular compartments after binding to HER2 on the cell membrane and, in particular, were in lysosomes since HApt was designed to traffic HER2 to this organelle.

To correlate nanoconstruct clustering with lysosome location, we stained lysosomes with LysoTracker Green DND-26 (Supporting Information); however, to avoid interference with lysosomal signals, we used Cy5 labels on HApt-AuNS. Figure 2b shows that the overlapping signals of Cy5 from HApt (red) with lysosomes (green) were higher for HApt-AuNS compared to free HApt, which suggests that AuNS can act as a nanocarrier for efficient delivery of aptamer into the targeted organelle.

***In Vitro* Therapeutic Response of HApt-AuNS *vs* Free HApt.** Next, we tested whether improved delivery efficiency and localization of HApt-AuNS were correlated with a biological response of cancer cells. Figure 3a shows that cell viability of SK-BR-3 decreased *ca.* 50% after treatment with HApt-AuNS for 24 h compared to free HApt, where the latter did not result in anticancer effects even after treatment for 5 days (Supporting Information Figure S7). Cell viability decreased continuously as HApt-AuNS incubation time increased from 24 h to 72 h (24 h: 59%, 48 h: 48%, 72 h: 38%). Although the HApt-induced HER2 degradation process is likely the same for free HApt and HApt-AuNS since the structure of HApt is preserved on the AuNS, the nanoconstruct showed much stronger anticancer effects in SK-BR-3. We hypothesize that dense packing and presentation of

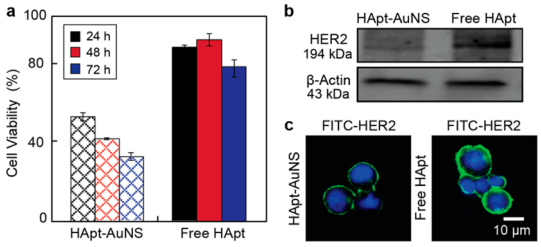


**Figure 3. HApt-AuNS show greater anticancer effects compared to free HApt. (a) Cell viability over 72 h for SK-BR-3 cells treated with HApt-AuNS and free HApt. Error bars were from 12 independent experiments. The concentration of HApt-AuNS was 2.5 nM, the same HApt concentration as free HApt (1 $\mu$M). Error bars represent seven independent experiments ($n$ = 7). (b) Protein detection of HER2 and $\beta$-actin using Western blot after 24 h treatment. HApt-AuNS had an intensity of 59.44 ($\pm$14.88), while free HApt has a band intensity of 142.27 ($\pm$12.96). The average intensity of three gel images was statistically analyzed by measuring the total intensity across the same area in each image. (c) HER2 stained by FITC-labeled anti-HER2 antibody is less after HApt-AuNS incubation compared to free HApt. In all images, the green signal represents HER2, and the blue signal is the nucleus. Cells were incubated with HApt-AuNS (2.5 nM) or 1 $\mu$M free HApt. The representative images were collected from fluorescence images of three independent experiments ($n$ = 3).**

HApt on AuNS provides a means to bind to multiple HER2 receptors. Importantly, this multivalency increases avidity to target cell-surface receptors[40] as well as induces the formation of receptor clusters on cell membranes.[41,42] Therefore, HApt-AuNS could improve not only delivery efficiency of HApt to target cancer cells but also the possibility to accumulate more HER2 into lysosomes, which can result in enhanced anticancer effects.

Because inhibition of cancer cell proliferation is from cell cycle arrest (cytostatic effect) and because cell death (cytotoxic effect) is induced by therapeutic agents,[43,44] we investigated whether there was a correlation between cell cycle and cell viability at three different times points (8, 16, and 24 h). Supporting Information Figure S8 shows that after 16 h incubation with HApt-AuNS, cell death occurred. Importantly, this time point is close to the doubling time (the time to complete a cell cycle) of proliferating SK-BR-3 cells

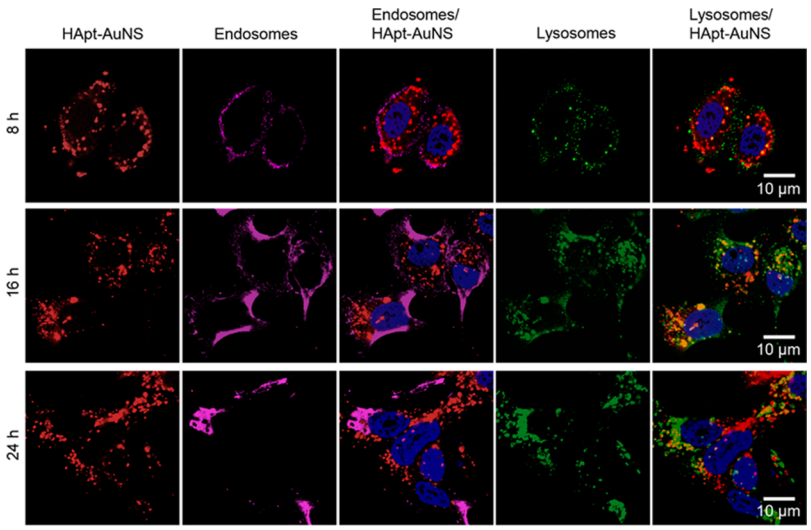


**Figure 4. ?A3B2 tlsb=-0.01w?>HApt-AuNS cluster sizes within lysosomes show a time-dependent increase. Confocal fluorescence images of SK-BR-3 cells after 8, 16, and 24 h treatments. Cy5-HApt-AuNS are red, immunostained endosomes with EEA-1 antibody are magenta, and lysosomes with LAMP-1 antibody are green. The scale bars in all images are 10 $\mu$m. The representative images were collected from fluorescence images of two independent experiments ($n$ = 2).**

(15 h).[45] To ensure robustness of the correlation as a function of time, we synchronized cell phase through serum deprivation in cell cycle analysis. We found that the transition of SK-BR-3 cells into G0/G1 phase increased *ca.* 1.2 times after 24 h incubation (Methods). In addition, the average ratio of cells in the G0/G1 phase increased continuously as a function of time (0 h: 77.8 $\pm$ 4.5%, 8 h: 81.0 $\pm$ 7.2%, 16 h: 89.9 $\pm$ 11.7%, 24 h: 91.9 $\pm$ 10.7%), suggesting that growth and proliferation in SK-BR-3 cells were inhibited.[46]

Because the biological activity of HApt is correlated with its ability to sort HER2 for lysosomal degradation,[25] we evaluated HER2 expression levels using both Western blot and fluorescence immunostaining (Supporting Information). Figure 3b indicates that the relative intensity of the HER2 band decreased *ca.* 2.4 times in HApt-AuNS-treated cells compared to free HApt-treated cells. Furthermore, fluorescence signals from HER2 markedly decreased when SK-BR-3 cells were incubated with HApt-AuNS (Figure 3c). These data support that the functionalization of HApt on AuNS can improve efficacy of HER2 degradation in cancer cells and that proliferation is decreased.

Because HER2 degradation occurs in lysosomes, we monitored subcellular locations of HER2-HApt-AuNS complexes as a function of time. To determine when the majority of nanoconstructs accumulated in lysosomes *via* the endocytosis pathway, we identified locations of HApt-AuNS in cells at the same time points as that in cell viability and cell cycle studies (8, 16, 24 h) (Figure 4). First, we stained early endosomes and lysosomes of SK-BR-3 cells by immunostaining to visualize the vesicles. Lysosome-associated membrane glycoprotein 1 (LAMP-1) and early endosome antigen 1 (EEA-1) were stained by anti-LAMP-1 antibody and anti-EEA-1 antibody, respectively. Next, we used both confocal and differential interference contrast (DIC) microscopy to identify the HER2-HApt-AuNS complexes based on Cy5-labeled HApt and Au contrast.[47] Overlaying fluorescence and DIC images, we observed that as incubation time increased from 8 h to 24 h, the HER2-HApt-AuNS complexes were farther inside the cells (Figure 4 and Supporting Information Figure S9). At 8 h, the Cy5 signal from the clusters overlapped with endosomal signals in the fluorescence images, which indicated clusters were in the endosomes. Lysosomal staining using LAMP-1 indicated minimal formation of lysosomes at this time point. At later times, such as 16 and 24 h, the fluorescence signals of lysosomes increased significantly and overlapped with the Cy5 label on HApt-AuNS (Figure 4). DIC images indicated that HER2-HApt-AuNS were also at similar intracellular locations (Supporting Information Figure S9). Almost no colocalization was observed between signals of endosomes and Cy5-HApt-AuNS at 16 and 24 h. In addition, we confirmed that the anisotropic AuNS shape was preserved in cells by transmission electron microscopy at incubation times (Supporting Information Figure S10). Taken together, the results support our hypothesis that HER2-HApt-AuNS complexes transfer from endosomes to lysosomes after HApt-AuNS binds to HER2 on the plasma membrane (Scheme 1).

We compared the sizes of HER2-HApt-AuNS clusters in SK-BR-3 and MCF-10A through DIC imaging and image analysis. The average cluster size was *ca.* 2.2 times larger in SK-BR-3 compared to MCF-10A after 24 h. Also, at 16 h, SK-BR-3 cells showed a significant increase in cluster size compared to the size at 8 h, while MCF-10A showed little increase (Supporting Information Figure S11). Hence, the clustering of HApt-AuNS in cells depends strongly on the cellular uptake *via* HER2-mediated endocytosis.

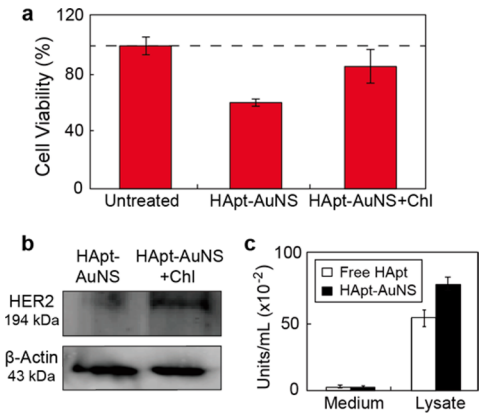


**Figure 5. Lysosomal function is involved in anticancer effects of HApt-AuNS. (a) Cell viability (MTS assay) after 24 h treatment of SK-BR-3 cells with HApt-AuNS (2.5 nM) and chloroquine (Chl). Error bars from 12 independent experiments. (b) HER2 analyzed by Western blot. The average intensity of the band for HApt-AuNS was 63.31 (±1.61), and that for HApt-AuNS with Chl was 120.05 (±22.39). The standard deviation was obtained from three experiments. (c) Acid phosphatase assay indicates enzyme activity after 24 h incubation of cells with free HApt (1 $\mu$M) and HApt-AuNS (2.5 nM). Error bars from eight independent experiments.**

**Correlating Lysosomal Activity, HER2 Degradation, and Cell Death.** During the endocytosis process, molecules transported to lysosomes[48,49] can be degraded by hydrolytic enzymes including proteases, nucleases, glycosidases, lipases, phospholipases, phosphatases, and sulfatases.[50,51] To determine whether the increased HER2 degradation and therapeutic efficacy from HApt-AuNS could be attributed to altered lysosomal activity, we tested whether degradation of HER2 would be affected if lysosomal function was compromised using chloroquine, a chemical that can passively diffuse into lysosomes and increase lysosomal pH, to disrupt lysosomal activity.[52] Figure 5a indicates that cells treated with chloroquine and then subjected to HApt-AuNS showed a 26% increase in cell viability compared to cells treated with the same concentration of HApt-AuNS and no chloroquine. Hence, lysosomal function is important for the effects of HApt-AuNS in our *in vitro* model. Moreover, the results support that HER2-HApt-AuNS complexes were delivered into targeted lysosomes based on HER2-mediated endocytosis and that HER2 degradation resulted in cell death. To examine whether increased cell viability after blocking lysosomal function would result in decreased HER2 degradation, we measured HER2 expression levels from cell lysates (Methods). Figure 5b shows that the HER2 band intensity increased by *ca*. 50% in cells with compromised lysosomal function; thus, HER2 is preserved (not degraded) even after cells were incubated with HApt-AuNS.

In addition, we found that volumetric changes of lysosomes were also related to lysosomal activity and the permeabilization of the lysosomal membrane. On the basis of literature,[24,51,53] we hypothesized that accumulation of nanoconstructs in lysosomes would increase volume and thus further increase lysosomal activity. Upregulation of lysosomal components such as proteases could accelerate HER2 degradation. Therefore, we tested whether accumulation of HER2-HApt-AuNS complexes in lysosomes affected lysosomal activity by comparing the levels of lysosomal marker enzymes.[54] We measured acid phosphatase, an acid hydrolase commonly in lysosomes,[55] from cell-cultured media and cell lysates after 24 h incubation of free HApt and HApt-AuNS. The assay demonstrated that HApt-AuNS induced a 1.5 (±0.2) times increase of acid phosphatase levels in cells compared to free HApt. Notably, in media, the levels of acid phosphatase were nearly the same in free HApt-treated cells (6.3 ± 1.3) and HApt-AuNS-treated cells (5.1 ± 1.2) (Figure 5c). Therefore, accumulation of HER2-HApt-AuNS in lysosomes can increase lysosomal activity besides the HApt-AuNS enhancing HER2 degradation compared to free HApt.

## CONCLUSION

We demonstrated that internalization of HApt-AuNS nanoconstructs *via* endocytosis can improve the lysosomal targeting efficiency of a DNA aptamer. Accumulation of HER2-HApt-AuNS complexes in lysosomes resulted in enhanced lysosomal activity, which was also correlated to accelerated degradation of HER2. As a result, increased HER2 downregulation induced cell death by blocking the function of HER2 and decreased cell proliferation by altering signaling pathways for growth. Nanoparticle carriers provide potential for enhancing targeting efficiency of drugs and for degrading overexpressed surface receptors in lysosomes. Moreover, the optical properties of AuNS can be used as a diagnostic to understand how HApt can function in cells by correlating DIC images of AuNS with the fluorescence signals of HApt as well as endosomal and lysosomal labels. We anticipate that the anisotropic structure of AuNS can be applied in photothermal therapy to enhance anticancer effects, especially since the localized surface plasmon resonance is in the near-infrared. These results suggest a strategy to design efficacious nanoconstructs by exploiting their accumulation in lysosomes and by enhancing therapeutic efficacy of lysosome-targeting drugs for preclinical studies.

## METHODS

**Preparation of HApt-AuNS Nanoconstruct.** Anti-HER2 aptamer (42 bp) with disulfide modification at the 5′-end (5′-(C6-S-S-C6)-GCA GCG GTG TGG GGG CAG CGG TGT GGG GGC AGC GGT GTG GGG-3′) was purchased from IDT DNA, Inc. HPLC-purified aptamer was dissolved in Millipore water (18.2 MΩ cm) to obtain 1 mM solutions. The disulfide bond was cleaved by adding 5 $\mu$L of 5 mM

tris(2-carboxyethyl)phosphine (TCEP) (Sigma-Aldrich) to 5 $\mu$L of the 1 mM aptamer solution. After 30 min, the thiolated aptamer solution was added to 10 mL of 0.3 nM AuNS (final concentration ratio of DNA:AuNS = 1600:1) and left overnight to form the nanoconstruct (HApt-AuNS).

**Tissue Culture for Cancer and Control Cell Lines.** The human breast carcinoma SK-BR-3 cell line (ATCC) was maintained in McCoy's medium (Gibco) supplemented with 10% fetal bovine serum (FBS) (Gibco). The human epithelial cell line MCF-10A (ATCC) was maintained in DMEM/F12 medium (Gibco) supplement with 10% horse serum (Invitrogen), 20 ng/mL epidermal growth factor (EGF) (Sigma-Aldrich), 0.5 mg/mL hydrocortisone (Sigma-Aldrich), 100 ng/mL cholera toxins (Sigma-Aldrich), and 10 $\mu$g/mL insulin (Sigma-Aldrich). The cells were cultured at 37 C with 5% $CO_2$ and plated in T25 flasks (VWR) with the aforementioned media.

**Cell Viability Measurement.** After incubation of cells ($1 \times 10^4$ cells/mL) with HApt-AuNS in a 96-well plate, the cell viability was measured using MTS assay solution (Promega). The absorbance of the reacted solution at 490 nm was recorded by a 96-well plate reader (Multiskan Spectrum, Thermo Scientific).

**Quantifying Number of HApt Strands on AuNS.** Cy3-labeled aptamer (5′-(C6-S-S-C6)-Cy3-GCA GCG GTG TGG GGG CAG CGG TGT GGG GGC AGC GGT GTG GGG-3′) was used to estimate the number of aptamers on each particle. Attachment of Cy5-HAptt and Cy3-HApt to the AuNS followed the same procedure as described previously. We centrifuged 500 $\mu$L of Cy3-labeled HApt-AuNS (Cy3-Apt-AuNS) at 13 500 rpm for 11 min. The supernatant was removed, and the nanoconstructs were suspended in 1 mL of 50 mM HEPES buffer. This process was repeated twice to eliminate unbound Cy3-HApt. Fluorescence-labeled nanoconstruct pellets were treated with 50 $\mu$L of 25 mM potassium cyanide (KCN) overnight to dissolve the Au core of nanoconstructs and release Cy3-HApt. Cy3 fluorescence intensity in KCN solution was measured using a NanoDrop spectrophotometer, and the concentration of HApt was determined based on the intensity of the Cy3 signal. The number of HApt was calculated by multiply the concentration of HApt with solution volume. Finally, the number of HApt was divided by the total number of AuNS in 1 mL. This fluorescent assay indicated that approximately 410 strands of HApt were conjugated on a single AuNS.

**Circular Dichroism Anlaysis.** The structure of free HApt and HApt-AuNS under the same buffer conditions (50 mM HEPES containing 10 mM NaCl) was analyzed by a CD spectrometer (JASCO). We used a 1 mm path length cuvette, which allowed a small volume of concentrated nanoconstructs solution to be measured. The CD spectra of nanoconstructs were also subtracted from background CD of AuNS in the same buffer.

**Quantification of Nanoconstruct Uptake in Cells.** Cells were plated in 24-well plates ($10^6$ cells/well) for 24 h, and then 2.5 nM HApt-AuNS in growth media was added to each well. The cells were incubated with the nanoconstructs for 24 h at 37 °C in a 5% $CO_2$ environment. After incubation, excess nanoconstructs were removed from the wells, and the cells were washed twice with ice cold PBS (Gibco). The cells were then harvested and suspended in 100 $\mu$L of PBS. The cells were counted using a hemocytometer before being digested for 4 h at 75 °C in an acid mixture containing 200 $\mu$L of 30% HCl (Sigma-Aldrich) and 86 $\mu$L of 70% $HNO_3$ (SigmaAldrich). After complete digestion of the AuNS, the solution was diluted with Millipore water to a final volume of 6 mL. The Au content was measured using ICP-MS.

**Confocal and DIC Imaging of Cy3- or Cy5-Labeled Nanoconstructs.** SK-BR-3 was plated on coverslips (BD Biosciences) ($10^4$ cells/coverslip) and cultured in their respective complete growth media. After 24 h of cell growth (37 °C, 5% $CO_2$), the media was replaced with fresh growth media containing 2.5 nM Cy3- or Cy5-labeled nanoconstructs. Cells were incubated with the nanoconstructs for 8, 16, and 24 h and then washed three times with PBS. The cells were fixed with 4% paraformaldehyde (Sigma-Aldrich) for 20 min followed by three washes with PBS. A drop of ProLong Gold Antifade reagent containing DAPI (Invitrogen) was used to mount each coverslip on a glass slide for confocal fluorescence and DIC imaging. Confocal imaging was performed on an inverted Zeiss Axio Observer Z1 confocal microscope with a 40× objective and Zen acquisition software, and DIC imaging was performed by an inverted Nikon Eclipse TE2000-E microscope.

**Immunofluorescence Staining.** Cells were plated on coverslips (BD Biosciences) ($10^4$ cells/coverslip) and cultured in their respective complete growth media. After treatment with HApt-AuNS, the coverslips were washed with PBS twice to remove all residual growth media. Cells were fixed with 4% paraformaldehyde for 10 min and permeabilized with 0.1% Triton X100 for 5 min. The coverslips containing fixed cells were then blocked with solution containing 1% BSA and 5% normal donkey serum for 1 h at room temperature. The cells were then incubated at 4 °C overnight with primary antibodies (1:200) in blocking solution (mouse anti-human LAMP-1 antibody (Santa Cruz) and goat anti-human EEA-1 antibody (Santa Cruz)). After overnight incubation, the coverslips were washed six times with PBS for a total of 1 h. Secondary antibodies in blocking solution were incubated with the coverslips for 1 h at room temperature (donkey anti-goat IgG Alexa 488 and donkey anti-mouse IgG Alexa 568). The coverslips were washed for 1 h with PBS, and cell nuclei were counterstained with DAPI. The coverslips were then mounted on glass slides using gold-antifade mounting media (Invitrogen).

**Staining of Cellular Structures.** Cells were plated on coverslips (BD Biosciences) ($10^4$ cells/coverslip) and cultured in their respective complete growth media. After cell incubation with 2.5 nM HApt-AuNS, the medium was removed from the dish and the prewarmed (37 °C) Lysotracker Green DND26 (Invitrogen)-containing medium was added. The cells were incubated for 30 min under growth conditions. Then, cells were fixed with 4% paraformaldehyde. A drop of ProLong Gold Antifade reagent containing DAPI (Invitrogen) was used to mount each coverslip on a glass slide for confocal fluorescence and DIC imaging.

**Immunoblotting of HER2.** SK-BR-3 cells ($5 \times 10^5$ cells/mL) were cultured on a six-well plate in complete medium for 24 h. Then, 2.5 nM HApt-AuNS and 1 $\mu$M free HApt in culture media were added to each well and incubated for 24 h. Cells were then collected and transferred to microcentrifuge tubes. For cell lysis, RIPA buffer (Pierce) was added and incubated for 30 min on ice. The protein amount was estimated by BCA assay (Bio-Rad). Next, an equal volume of sample buffer (125 mM Tris pH 6.8, 4% SDS, 10% glycerol, 0.006% bromophenol blue, and 1.8% ss-mercaptoethanol) was added to all samples, and the resulting solution was boiled for 3−5 min. A 15 $\mu$g amount of total proteins from cells was loaded in each well of a protein precast gel (Bio-Rad). After electrophoresis at 120 V and 60 min, the proteins were transferred from the gel to a PVDF membrane at 1 A constant current for 1 h in transfer buffer (Thermo Fisher). The blot from the transfer apparatus was removed and immediately placed into blocking buffer (5% nonfat dry milk, 10 mM Tris pH 7.5, 100 mM NaCl, and 0.1% Tween 20). After blocking for 1 h at room temperature, the membrane was incubated with primary anti-HER2 antibody (mouse) and anti-$\beta$ actin (mouse) (Santa Cruz) overnight at 4 °C. After incubation with primary antibody solution, the membrane was twice washed (10 mM Tris pH 7.5, 100 mM NaCl, and 0.1% Tween 20). Then, the membrane was incubated with alkaline phosphatase (AP)-conjugate anti-mouse IgG (secondary antibody) diluted with 5% nonfat dry milk solution at room temperature. After 1 h incubation, the antibody solution was removed and the membrane was washed three times by washing buffer (10 mM Tris pH 7.5, 100 mM NaCl, 0.1% Tween 20). Finally, the band signal of proteins on the membrane was developed by enhanced chemifluorescence substrate (GE Healthcare) and visualized by a Typhoon PhosphorImager (GE Healthcare). The amount of each protein in the blots was determined by counting the total number of pixels in each band (integrated density value) with ImageJ.

**Chloroquine Treatment.** SK-BR-3 on 96-well and six-well plates was incubated with culture media containing 0.01 $\mu$M chloroquine (Chl) for 24 h. After treatment of cells with Chl, 2.5 nM-HApt-AuNS was added into the cells on the well and incubated with the cells. After 24 h incubation, the media was discarded, and 100 $\mu$L of new media and MTS assay solution added into the 96-well plate to test the viability. For HER2 detection, cells were

harvested and were lysed. Immunoblotting to HER2 followed the same procedure as described previously.

**Acid Phosphatase Assay.** SK-BR-3 on the 96-well plate was incubated with 1 $\mu$M free HApt and 2.5 nM-HApt-AuNS nanoconstruct for 24 h. The substrate solution, 4-nitrophenyl phosphate (Sigma-Aldrich), was dissolved in 5 mL of the citrate buffer solution and equilibrated to 37 °C before using. A 50 $\mu$L amount of substrate solution was mixed with 50 $\mu$L of the cell lysate sample. A blank reaction (50 $\mu$L of substrate solution with 50 $\mu$L of citrate buffer) was run in parallel to account for the 4-nitrophenylphosphate that hydrolyzes spontaneously during the incubation time. For a positive control, 50 $\mu$L of substrate solution was incubated with 48 $\mu$L of citrate buffer and 2 $\mu$L of acid phosphatase enzymes. The 96-well plate was mixed using a horizontal shaker, and the plate incubated for 10 min at 37 °C. The reactions were stopped by adding 0.2 mL of a 0.5 N NaOH solution to the wells. The absorption of colored solution was measured at 405 nm.

*Conflict of Interest:* The authors declare no competing financial interest.

*Acknowledgment.* This work was supported by Cancer Center Nanotechnology Excellence (CCNE) of the NIH National Cancer Institute at Northwestern University (U54 CA151880), a National Institutes of Health (NIH) Director's Pioneer Award (DP1 EB016540), and the H Foundation Cancer Research Fund and Malkin Scholar Award by the Robert H. Lurie Comprehensive Cancer Center at Northwestern University. D.H.M.D. is supported by Post Graduate Program in Cutaneous Biology (NIH T32 AR060710).

*Supporting Information Available:* The Supporting Information is available free of charge on the ACS Publications website at DOI: 10.1021/acsnano.5b05138.

HApt-AuNS nanoconstruct characterization and stability test of nanoconstruct in FBS. SK-BR-3 cell viability test at different concentrations of HApt-AuNS and at different incubation times with free HApt. ICP-MS analysis of SK-BR-3 and MCF-10A after 24 h incubation. MCF-10A viability test after incubation of cells with nanoconstruct for 72 h. Competition assay of SK-BR-3 with free HApt and HApt-AuNS. Cell cycle analysis and optical images of cells at different time points. TEM images of HApt-AuNS in cells at different time points. Statistical analysis for cluster size in MCF-10A and SK-BR-3 (PDF)

## REFERENCES AND NOTES

1. Petros, R. A.; DeSimone, J. M. Strategies in the Design of Nanoparticles for Therapeutic Applications. *Nat. Rev. Drug Discovery* **2010**, *9*, 615–627.
2. Sapsford, K. E.; Algar, W. R.; Berti, L.; Gemmill, K. B.; Casey, B. J.; Oh, E.; Stewart, M. H.; Medintz, I. L. Functionalizing Nanoparticles with Biological Molecules: Developing Chemistries that Facilitate Nanotechnology. *Chem. Rev.* **2013**, *113*, 1904–2074.
3. Daniel, M.-C.; Astruc, D. Gold Nanoparticles: Assembly, Supramolecular Chemistry, Quantum-Size-Related Properties, and Applications toward Biology, Catalysis, and Nanotechnology. *Chem. Rev.* **2004**, *104*, 293–346.
4. Dykman, L.; Khlebtsov, N. Gold Nanoparticles in Biomedical Applications: Recent Advances and Perspectives. *Chem. Soc. Rev.* **2012**, *41*, 2256–2282.
5. Xie, J.; Lee, S.; Chen, X. Nanoparticle-Based Theranostic Agents. *Adv. Drug Delivery Rev.* **2010**, *62*, 1064–1079.
6. Ghosh, P.; Han, G.; De, M.; Kim, C. K.; Rotello, V. M. Gold Nanoparticles in Delivery Applications. *Adv. Drug Delivery Rev.* **2008**, *60*, 1307–1315.
7. Dam, D. H. M.; Lee, R. C.; Odom, T. W. Improved *in Vitro* Efficacy of Gold Nanoconstructs by Increased Loading of G-quadruplex Aptamer. *Nano Lett.* **2014**, *14*, 2843–2848.
8. Dam, D. H. M.; Culver, K. S. B.; Odom, T. W. Grafting Aptamers onto Gold Nanostars Increases *in Vitro* Efficacy in a Wide Range of Cancer Cell Types. *Mol. Pharmaceutics* **2014**, *11*, 580–587.
9. Dam, D. H. M.; Lee, J. H.; Sisco, P. N.; Co, D. T.; Zhang, M.; Wasielewski, M. R.; Odom, T. W. Direct Observation of Nanoparticle–Cancer Cell Nucleus Interactions. *ACS Nano* **2012**, *6*, 3318–3326.
10. Rotz, M. W.; Culver, K. S. B.; Parigi, G.; MacRenaris, K. W.; Luchinat, C.; Odom, T. W.; Meade, T. J. High Relaxivity Gd(III)–DNA Gold Nanostars: Investigation of Shape Effects on Proton Relaxation. *ACS Nano* **2015**, *9*, 3385–3396.
11. Dam, D. H. M.; Culver, K. S. B.; Kandela, I.; Lee, R. C.; Chandra, K.; Lee, H.; Mantis, C.; Ugolkov, A.; Mazar, A. P.; Odom, T. W. Biodistribution and *in Vivo* Toxicity of Aptamer-Loaded Gold Aanostars. *Nanomedicine* **2015**, *11*, 671–679.
12. Wang, A. Z.; Langer, R.; Farokhzad, O. C. Nanoparticle Delivery of Cancer Drugs. *Annu. Rev. Med.* **2012**, *63*, 185–198.
13. Lee, H.; Odom, T. W. Controlling Ligand Density on Nanoparticles as a Means to Enhance Biological Activity. *Nanomedicine* **2015**, *10*, 177–180.
14. Ha, J. W.; Fang, N. Defocused Differential Interference Contrast Microscopy Imaging of Single Plasmonic Anisotropic Nanoparticles. *Chem. Commun.* **2014**, *50*, 5500–5502.
15. Sajanlal, P. R.; Sreeprasad, T. S.; Samal, A. K.; Pradeep, T. Anisotropic Nanomaterials: Structure, Growth, Assembly, and Functions. *Nano Rev.* **2011**, *2*, 3402.
16. Dam, D. H. M.; Lee, H.; Lee, R. C.; Kim, K. H.; Kelleher, N. L.; Odom, T. W. Tunable Loading of Oligonucleotides with Secondary Structure on Gold Nanoparticles through a pH-Driven Method. *Bioconjugate Chem.* **2015**, *26*, 279–285.
17. Panyam, J.; Zhou, W.-Z.; Prabha, S.; Sahoo, S. K.; Labhasetwar, V. Rapid Endo-Lysosomal Escape of Poly(dl-lactide-co-glycolide) Nanoparticles: Implications for Drug and Gene Delivery. *FASEB J.* **2002**, *16*, 1217–1226.
18. Torchilin, V. P.; Rammohan, R.; Weissig, V.; Levchenko, T. S. TAT Peptide on the Surface of Liposomes Affords Their Efficient Intracellular Delivery Even at Low Temperature and in the Presence of Metabolic Inhibitors. *Proc. Natl. Acad. Sci. U. S. A.* **2001**, *98*, 8786–8791.
19. Wattiaux, R.; Laurent, N.; Wattiaux-De Coninck, S.; Jadot, M. Endosomes, Lysosomes: Their Implication in Gene Transfer. *Adv. Drug Delivery Rev.* **2000**, *41*, 201–208.
20. Byrne, J. D.; Betancourt, T.; Brannon-Peppas, L. Active Targeting Schemes for Nanoparticle Systems in Cancer Therapeutics. *Adv. Drug Delivery Rev.* **2008**, *60*, 1615–1626.
21. Zhong, Y.; Meng, F.; Deng, C.; Zhong, Z. Ligand-Directed Active Tumor-Targeting Polymeric Nanoparticles for Cancer Chemotherapy. *Biomacromolecules* **2014**, *15*, 1955–1969.
22. Moradi, E.; Vllasaliu, D.; Garnett, M.; Falcone, F.; Stolnik, S. Ligand Density and Clustering Effects on Endocytosis of Folate Modified Nanoparticles. *RSC Adv.* **2012**, *2*, 3025–3033.
23. Bareford, L. M.; Swaan, P. W. Endocytic Mechanisms for Targeted Drug Delivery. *Adv. Drug Delivery Rev.* **2007**, *59*, 748–758.
24. Domenech, M.; Marrero-Berrios, I.; Torres-Lugo, M.; Rinaldi, C. Lysosomal Membrane Permeabilization by Targeted Magnetic Nanoparticles in Alternating Magnetic Fields. *ACS Nano* **2013**, *7*, 5091–5101.
25. Mahlknecht, G.; Maron, R.; Mancini, M.; Schechter, B.; Sela, M.; Yarden, Y. Aptamer to ErbB-2/HER2 Enhances Degradation of the Target and Inhibits Tumorigenic Growth. *Proc. Natl. Acad. Sci. U. S. A.* **2013**, *110*, 8170–8175.
26. Rusnak, D. W.; Alligood, K. J.; Mullin, R. J.; Spehar, G. M.; Arenas-Elliott, C.; Martin, A. M.; Degenhardt, Y.; Rudolph, S. K.; Haws, T. F., Jr; Hudson-Curtis, B. L.; et al. Assessment of Epidermal Growth Factor Receptor (EGFR, ErbB1) and HER2 (ErbB2) Protein Expression Levels and Response to Lapatinib (Tykerb®, GW572016) in an Expanded Panel of Human Normal and Tumour Cell Lines. *Cell Proliferation* **2007**, *40*, 580–594.
27. Van de Broek, B.; Devoogdt, N.; D'Hollander, A.; Gijs, H.-L.; Jans, K.; Lagae, L.; Muyldermans, S.; Maes, G.; Borghs, G. Specific Cell Targeting with Nanobody Conjugated Branched Gold Nanoparticles for Photothermal Therapy. *ACS Nano* **2011**, *5*, 4319–4328.

28. Corsi, F.; Fiandra, L.; De Palma, C.; Colombo, M.; Mazzucchelli, S.; Verderio, P.; Allevi, R.; Tosoni, A.; Nebuloni, M.; Clementi, E.; et al. HER2 Expression in Breast Cancer Cells Is Downregulated Upon Active Targeting by Antibody-Engineered Multifunctional Nanoparticles in Mice. *ACS Nano* **2011**, *5*, 6383–6393.
29. K. C., R. B.; Chandrashekaran, V.; Cheng, B.; Chen, H.; Peña, M. M. O.; Zhang, J.; Montgomery, J.; Xu, P. Redox Potential Ultrasensitive Nanoparticle for the Targeted Delivery of Camptothecin to HER2-Positive Cancer Cells. *Mol. Pharmaceutics* **2014**, *11*, 1897–1905.
30. Roh, H.; Pippin, J.; Drebin, J. A. Down-Regulation of HER2/neu Expression Induces Apoptosis in Human Cancer Cells That Overexpress HER2/neu. *Cancer Res.* **2000**, *60*, 560–565.
31. Münster, P. N.; Marchion, D. C.; Basso, A. D.; Rosen, N. Degradation of HER2 by Ansamycins Induces Growth Arrest and Apoptosis in Cells with HER2 Overexpression via a HER3, Phosphatidylinositol 3′-Kinase-AKT-dependent Pathway. *Cancer Res.* **2002**, *62*, 3132–3137.
32. Canton, I.; Battaglia, G. Endocytosis at the Nanoscale. *Chem. Soc. Rev.* **2012**, *41*, 2718–2739.
33. Jiang, W.; Kim, B. Y. S.; Rutka, J. T.; Chan, W. C. W. Nanoparticle-Mediated Cellular Response is Size-Dependent. *Nat. Nanotechnol.* **2008**, *3*, 145–150.
34. Verma, A.; Stellacci, F. Effect of Surface Properties on Nanoparticle−Cell Interactions. *Small* **2010**, *6*, 12–21.
35. Brigger, I.; Dubernet, C.; Couvreur, P. Nanoparticles in Cancer Therapy and Diagnosis. *Adv. Drug Delivery Rev.* **2002**, *54*, 631–651.
36. Gao, H.; Yang, Z.; Zhang, S.; Cao, S.; Shen, S.; Pang, Z.; Jiang, X. Ligand Modified Nanoparticles Increases Cell Uptake, Alters Endocytosis and Elevates Glioma Distribution and Internalization. *Sci. Rep.* **2013**, *3*, 2534.
37. Ménard, S.; Casalini, P.; Campiglio, M.; Pupa, S.; Agresti, R.; Tagliabue, E. HER2 Overexpression in Various Tumor Types, Focussing on Its Relationship to the Development of Invasive Breast Cancer. *Ann. Oncol.* **2001**, *12*, S15–S19.
38. Tanner, M.; Hollmén, M.; Junttila, T. T.; Kapanen, A. I.; Tommola, S.; Soini, Y.; Helin, H.; Salo, J.; Joensuu, H.; Sihvo, E.; et al. Amplification of HER-2 in Gastric Carcinoma: Association with Topoisomerase IIα Gene Amplification, Intestinal Type, Poor Prognosis and Sensitivity to Trastuzumab. *Ann. Oncol.* **2005**, *16*, 273–278.
39. Ramljak, D.; Romanczyk, L. J.; Metheny-Barlow, L. J.; Thompson, N.; Knezevic, V.; Galperin, M.; Ramesh, A.; Dickson, R. B. Pentameric Procyanidin from Theobroma Cacao Selectively Inhibits Growth of Human Breast Cancer Cells. *Mol. Cancer Ther.* **2005**, *4*, 537–546.
40. Wang, J.; Tian, S.; Petros, R. A.; Napier, M. E.; DeSimone, J. M. The Complex Role of Multivalency in Nanoparticles Targeting the Transferrin Receptor for Cancer Therapies. *J. Am. Chem. Soc.* **2010**, *132*, 11306–11313.
41. Elias, D. R.; Poloukhtine, A.; Popik, V.; Tsourkas, A. Effect of Ligand Density, Receptor Density, and Nanoparticle Size on Cell Targeting. *Nanomedicine* **2013**, *9*, 194–201.
42. Abulrob, A.; Lu, Z.; Baumann, E.; Vobornik, D.; Taylor, R.; Stanimirovic, D.; Johnston, L. J. Nanoscale Imaging of Epidermal Growth Factor Receptor Clustering: Effects of Inhibitors. *J. Biol. Chem.* **2010**, *285*, 3145–3156.
43. Shapiro, G. I.; Harper, J. W. Anticancer Drug Targets: Cell Cycle and Checkpoint Control. *J. Clin. Invest.* **1999**, *104*, 1645–1653.
44. Binková, B.; Giguère, Y.; Rössner, P., Jr; Dostál, M.; Šrám, R. J. The Effect of Dibenzo[a,l]pyrene and Benzo[a]pyrene on Human Diploid Lung Fibroblasts: the Induction of DNA Adducts, Expression of p53 and p21WAF1 Proteins and Cell Cycle Distribution. *Mutat. Res., Genet. Toxicol. Environ. Mutagen.* **2000**, *471*, 57–70.
45. Lee, E. A.; Keutmann, M. K.; Dowling, M. L.; Harris, E.; Chan, G.; Kao, G. D. Inactivation of the Mitotic Checkpoint as a Determinant of the Efficacy of Microtubule-Targeted Drugs in Killing Human Cancer Cells. *Mol. Cancer Ther.* **2004**, *3*, 661–669.
46. Vermeulen, K.; Van Bockstaele, D. R.; Berneman, Z. N. The Cell Cycle: A Review of Regulation, Deregulation and Therapeutic Targets in Cancer. *Cell Proliferation* **2003**, *36*, 131–149.
47. Khlebtsov, N.; Dykman, L.; Khlebtsov, B.; Staroverov, S.; Shirokov, A.; Matora, L.; Khanadeev, V.; Pylaev, T.; Tsyganova, N.; Terentyuk, G.; Bogatyrev, V. Analytical and Theranostic Applications of Gold Nanoparticles and Multifunctional Nanocomposites. *Theranostics* **2013**, *3*, 167–180.
48. Neun, B.; Stern, S. Monitoring Lysosomal Activity in Nanoparticle-Treated Cells. In *Characterization of Nanoparticles Intended for Drug Delivery*; McNeil, S. E., Ed.; Humana Press, 2011; pp 207−212.
49. Kim, J. A.; Aberg, C.; Salvati, A.; Dawson, K. A. Role of Cell Cycle on the Cellular Uptake and Dilution of Nanoparticles in a Cell Population. *Nat. Nanotechnol.* **2011**, *7*, 62–68.
50. Zabirnyk, O.; Yezhelyev, M.; Seleverstov, O. Nanoparticles as a Novel Class of Autophagy Activators. *Autophagy* **2007**, *3*, 278–281.
51. Kroemer, G.; Jaattela, M. Lysosomes and Autophagy in Cell Death Control. *Nat. Rev. Cancer* **2005**, *5*, 886–897.
52. Rubinsztein, D. C.; Gestwicki, J. E.; Murphy, L. O.; Klionsky, D. J. Potential Therapeutic Applications of Autophagy. *Nat. Rev. Drug Discovery* **2007**, *6*, 304–312.
53. Boya, P.; Kroemer, G. Lysosomal Membrane Permeabilization in Cell Death. *Oncogene* **2008**, *27*, 6434–6451.
54. Hønsi, T. G.; Stenersen, J. Activity and Localisation of the Lysosomal Marker Enzymes Acid Phosphatase, N-acetyl-β-d-glucosaminidase, and β-galactosidase in the Earthworms Eisenia fetida and E. veneta. *Comp. Biochem. Physiol., Part B: Biochem. Mol. Biol.* **2000**, *125*, 429–437.
55. Suter, A.; Everts, V.; Boyde, A.; Jones, S. J.; Lüllmann-Rauch, R.; Hartmann, D.; Hayman, A. R.; Cox, T. M.; Evans, M. J.; Meister, T.; et al. Overlapping Functions of Lysosomal Acid Phosphatase (LAP) and Tartrate-Resistant Acid Phosphatase (Acp5) Revealed by Doubly Deficient Mice. *Development* **2001**, *128*, 4899–4910.